# Experimental Study of Flow-Induced Noise from Two Side-by-Side Cylinders

Reza Maryami*
Oklahoma State University, Stillwater, Oklahoma 74078
Paul Abromeit†
Brandenburg University of Technology Cottbus–Senftenberg, 03046 Cottbus, Germany
Chenghao Yang‡
Hefei University of Technology, 230009 Hefei, Anhui, People's Republic of China
Thomas F. Geyer§
German Aerospace Center (DLR), 03046 Cottbus, Germany
and
Brian R. Elbing¶
Oklahoma State University, Stillwater, Oklahoma 74078

https://doi.org/10.2514/1.J066755



**Flow around two closely spaced cylinders in a side-by-side configuration is a canonical aeroacoustic problem in aerospace systems such as landing gear struts. The aerodynamic interaction between the cylinders strongly affects surface pressure fluctuations and aerodynamic noise generation, motivating detailed studies. In this work, the near-field surface pressure and far-field noise of two identical circular cylinders were experimentally investigated at $Re = 3.0 \times 10^4$ for center-to-center spacings $T$ ranging from 1.2 to 3 times the cylinder diameter $D$. Surface pressure fluctuations were measured in both the spanwise and azimuthal directions using miniature transducers, while far-field noise was captured with a set of microphones. Except for spacing ratios close to $T/D = 3$, which behaved similarly to a single cylinder, the side-by-side arrangements exhibited reduced tonal noise, with the most pronounced attenuation at $T/D = 1.2$. This reduction was attributed to suppression of surface pressure fluctuations and their spanwise correlation over shorter lengths. At $T/D = 1.2$, multiple tones also appeared, with frequencies both lower and higher than the dominant tone of the single cylinder. Additionally, the stagnation and other critical points around the cylinders shifted by approximately 20° (clockwise for the lower and counterclockwise for the upper cylinder) resulting in an elliptical surface pressure distribution, pronounced gap-flow deflection, and a highly unsteady, asymmetric wake.**

## I. Introduction

CYLINDERLIKE structures are widely encountered in aerospace systems, such as landing-gear struts, antenna masts, heat exchangers, and support structures. In these configurations, unsteady flow phenomena, particularly von-Kármán vortex shedding, can generate significant aerodynamic noise that adversely affects vehicle performance, passenger comfort, and environmental noise compliance. Understanding the underlying mechanisms of noise generation, including the coupling between wake dynamics, unsteady surface pressure, and acoustic radiation, is essential for developing effective noise mitigation and flow control strategies. Although the flow and noise characteristics of a single cylinder have been extensively documented in both laminar and turbulent regimes [1,2], the acoustic behavior of multiple-cylinder arrangements remains considerably more complex and less understood. When two or more cylinders are placed in proximity, their shear layers and wakes interact, producing interference effects, synchronized vortex shedding, and amplified tonal noise that are highly sensitive to spacing and flow conditions. To investigate these interactions in a controlled manner, the simplest multiple-cylinder configuration in crossflow consists of two circular cylinders of equal diameter $D$ as illustrated in Fig. 1. The two most widely studied arrangements are tandem and side-by-side configurations, shown in Figs. 1a and 1b, respectively, defined by the center-to-center longitudinal and transverse spacings $L$ and $T$. The most general configuration is the staggered arrangement, depicted in Fig. 1c, which is commonly encountered in practical applications, as oncoming flow is rarely perfectly aligned with or perpendicular to the line connecting cylinder centers. The staggered geometry is described by the center-to-center pitch $P$ and the angle of incidence $\alpha$ between the flow direction and the line connecting the cylinder centers. The three primary parameters governing the flow and aerodynamic behavior in multiple-cylinder arrangements are 1) the spacing between cylinders, 2) their orientation in the $x$–$y$ plane relative to the oncoming flow, and 3) the Reynolds number $Re$. In addition to these, factors such as inflow turbulence and surface characteristics can also influence the aerodynamic response.

As comprehensively reviewed by Zdravkovich [3–5], with more recent overviews by Sumner [6] and Zhou and Alam [7], the fluid dynamics of multiple-cylinder configurations have been extensively studied. These studies provide insight into the underlying flow physics and the classification of distinct flow regimes. For two-cylinder configurations in steady cross-flow, Zdravkovich [4] classified interactions into two primary types based on relative positioning:

1) Wake interference is one configuration, which occurs when the downstream cylinder is partially or fully immersed in the upstream cylinder's wake. This is typically observed in tandem configurations (Fig. 1a), where merged shear layers suppress vortex formation from the upstream cylinder.

Presented as Paper 2025-3690 at the AIAA Aviation Forum and ASCEND 2025, Las Vegas, NV, July 21–25, 2025.; received 20 December 2025; accepted for publication 30 April 2026; published online 26 August 2026. 

*Adjunct Assistant Professor, School of Mechanical & Aerospace Engineering; r.maryami@okstate.edu.

†Research Assistant, Chair of Electrified Aero Engines.

‡Ph.D. Student, Institute of Sound and Vibration Research.

§Head of Department, Institute of Electrified Aero Engines; formerly Technical Acoustics Group, Brandenburg University of Technology Cottbus-Senftenberg; thomas.geyer@dlr.de.

¶Professor, School of Mechanical & Aerospace Engineering; elbing@okstate.edu.

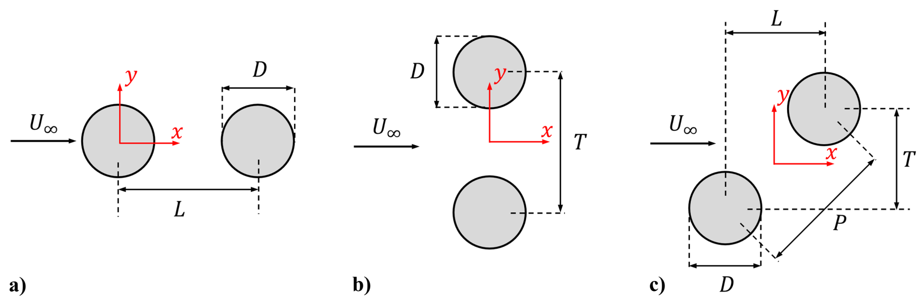


**Fig. 1 Configurations of two equal-diameter circular cylinders in cross-flow: a) tandem, b) side by side, and c) staggered.**

2) Proximity interference is the other configuration, which arises when closely spaced cylinders do not influence each other's wakes. This occurs in side-by-side arrangements (Fig. 1b) and often leads to synchronized vortex shedding. Gu and Sun [8] extended this classification to staggered configurations (Fig. 1c). They introduced wake, shear-layer, and neighborhood interference to capture more complex interactions. In addition to relative positioning, other criteria, such as vortex shedding frequencies [9], static surface pressure distributions [10], and mean lift and drag forces [11], have been used to characterize flow regimes [6]. However, relying solely on these measurements can be misleading in unsteady flows [6]. Hence, using flow visualization as the most effective approach for identifying distinct patterns, Igarashi [10] identified up to eight patterns for tandem cylinders, and Sumner et al. [12] reported nine distinct regimes for staggered arrangements.

Although the aerodynamic noise generated by multiple-cylinder configurations has not been explored as extensively as their flow dynamics, several studies have addressed this topic. For instance, in a tandem cylinder arrangement, Hutcheson and Brooks [13] demonstrated that the peak sound pressure level (SPL) exceeds that of a single cylinder in the coupled vortex street regime but becomes lower in the no-reattachment regime. In a related study, Lockard et al. [14] showed that the downstream cylinder dominates the acoustic radiation, producing a directivity pattern similar to that of an isolated cylinder. This directivity trend was further confirmed by Hutcheson et al. [15], who also reported that the Strouhal number $St$ increases with the spacing ratio $L/D$ and remains nearly constant with increasing flow speed when no regime transition occurs. Additionally, the peak SPL was found to scale with the sixth power of the flow Mach number and to increase with $L/D$ when variations in spacing induced a regime change. In contrast, for side-by-side and staggered cylinders, the number of studies remains very limited. Hutcheson and Brooks conducted one of the few investigations on side-by-side cylinders, showing that the peak SPL and $St$ are comparable to those of a single cylinder when the spacing corresponds to the coupled-wake regime. Reducing the gap between the cylinders led to a 20–25 dB decrease in peak SPL, while the noise directivity remained consistent with a dipole pattern. For staggered cylinders, Geyer and Enghardt [16] performed one of the only available experimental studies, examining tonal noise for two spacing ratios ($L/D = 2.0$ and 3.7). For the wide spacing, a single tonal peak associated with vortex shedding appeared at low angles of incidence, while increasing the angle to approximately 25 to 40 deg produced a second peak, indicating bistable behavior. In contrast, for the moderate spacing, a clear vortex-shedding tone was observed only at intermediate angles (20 to 80 deg), with multiple high-frequency tones occurring instead of a distinct secondary peak.

It is well established that, for a single cylinder, surface pressure fluctuations are key contributors both to far-field noise [17–22] and to structural vibrations through the generation of unsteady lift and drag forces [17–19,23,24]. In particular, Maryami and Liu [20] demonstrated that, in addition to direct acoustic radiation from the wake to the far field due to vortex shedding, the oscillating wake flow induces feedback signals that generate surface pressure fluctuations, especially at the top and bottom sides of the cylinder. These fluctuations are the primary source of unsteady lift, which subsequently produces scattered acoustic waves from the cylinder surface to the far field. Building on insights from single-cylinder flows, near-field surface pressure analyses of multicylinder configurations are essential for understanding aerodynamic noise. However, research has predominantly focused on tandem cylinders [14,15,25–28], largely to elucidate noise generation mechanisms relevant to landing gear. Lockard et al. [14] showed that surface pressure fluctuations on the upstream cylinder, primarily due to vortex shedding, are weaker than those on the downstream cylinder, where wake interactions significantly amplify the fluctuations, explaining the dominant acoustic radiation from the downstream cylinder. Jenkins et al. [25] reported that at a spacing of $L/D = 1.432$, the near-surface pressure spectra of both cylinders are entirely broadband, whereas increasing the spacing to $L/D = 3.7$ produces tonal peaks at the fundamental vortex-shedding frequency and its second harmonic. Extending this work, Maryami et al. [28] investigated near-field surface pressure fluctuations over a broader spacing range ($L/D = 1.432$–6) and found that spacing strongly affects surface pressure behavior: at subcritical spacing ($L/D < 3$–3.7), wake interactions enhance tonal peaks on the downstream cylinder and introduce unexpected tonal content at the upstream cylinder base ($\theta = 180$ deg), while at or above the critical spacing ($L/D \geq 3$–3.7), both cylinders exhibit pressure characteristics similar to a single cylinder, indicating minimal hydrodynamic interference. For other multicylinder configurations, near-field surface pressure characteristics have only been investigated for side-by-side cylinders in a recent experimental study by Maryami et al. [29], which demonstrated that the interaction between two side-by-side cylinders strongly depends on their spacing: close proximity induces significant gap-flow deflection and asymmetric vortex shedding, while larger spacings restore near-isolated-cylinder behavior.

This brief overview highlights that, although numerous studies have investigated the fluid dynamics of multicylinder configurations, research on near-field surface pressure and far-field noise has been largely confined to tandem arrangements. Investigations involving side-by-side and staggered cylinders remain extremely limited, particularly those focusing on near-field surface pressure. To date, no experimental or numerical studies have systematically characterized the near-field pressure fluctuations in conjunction with far-field noise for these configurations, despite their high relevance to practical engineering applications. Addressing this critical gap, the present experimental study provides a detailed characterization of surface pressure fluctuations around side-by-side cylinders and elucidates their relationship to far-field noise, offering new insights into the underlying flow–acoustic coupling mechanisms.

## II. Experimental Setup

### A. Wind-Tunnel Configuration

Near-field surface pressure measurements were carried out in the blowdown subsonic wind tunnel at Yazd University [30]. The wind tunnel features a working section measuring 460 mm × 460 mm with a length of 2400 mm, as illustrated in Fig. 2a. It is capable of operating at speeds up to 25 m/s, with a freestream turbulence intensity below 0.3% during experiments. The tunnel is powered by a forward-blade centrifugal fan, selected for its low broadband and tonal noise characteristics. To further improve its acoustic performance, the internal walls of the test section were replaced with stretched Kevlar sheets backed by a 15 cm thick porous layer,

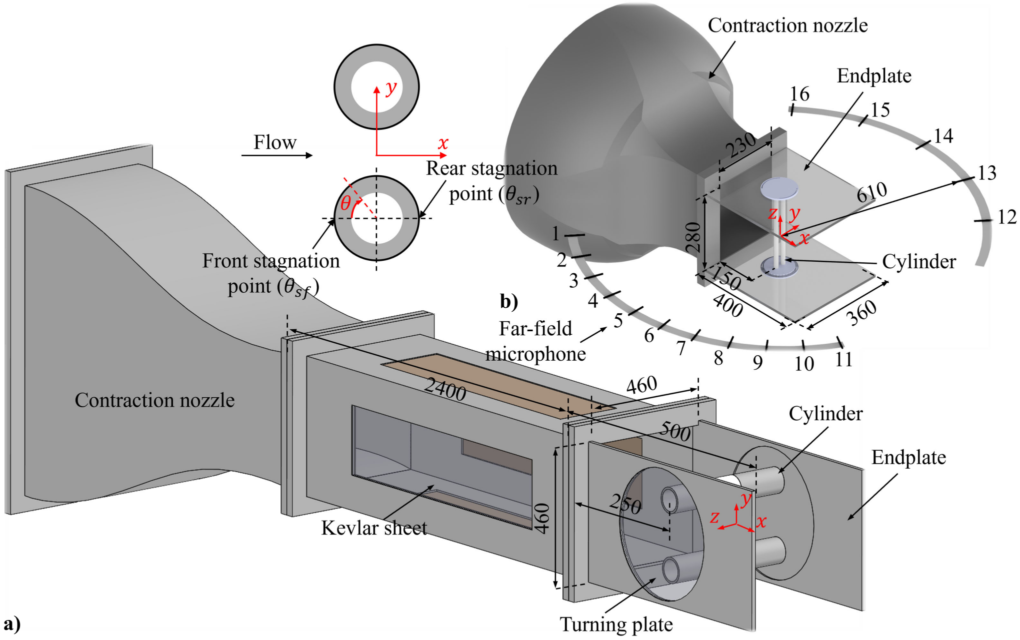


**Fig. 2 Schematic of the wind-tunnel facilities: a) Yazd University setup for unsteady surface pressure measurements and b) Brandenburg University setup for far-field acoustic measurements with coordinate system. The azimuthal angle $\theta$ is defined in the cylinder cross-sectional plane and measured clockwise from the front stagnation point ($\theta_{sf}$) in configuration part a. Dimensions are given in millimeters.**

which effectively reduced the fan-induced background noise by approximately 20 dB across a broad frequency range. In addition to the use of Kevlar sheets for noise reduction, the test cylinders were positioned 250 mm downstream of the wind-tunnel exit, mounted between two parallel laser-cut end plates, each measuring 500 mm in length, attached to the working section's sides. This configuration was designed to prevent contamination of the measurements by fan noise.

To complement these experiments, far-field acoustic measurements were conducted in the small aeroacoustic open-jet wind tunnel at the Brandenburg University of Technology Cottbus–Senftenberg [31]. As shown in Fig. 2b, this facility features a rectangular nozzle exit measuring 280 mm × 230 mm. The cylinders were positioned 150 mm downstream of the nozzle exit between acrylic end plates with dimensions of 400 mm × 360 mm. The sidewalls, back wall, and floor of the test section were lined with acoustic foam to create a quasi-anechoic environment for frequencies above approximately 100 Hz.

To enable the side-by-side configuration in both setups, two turning plates were used to adjust the cylinder orientations. The center-to-center spacing between the cylinders was set to $T/D = 1.2$, 2, and 3. For each configuration, the coordinate system was centered midway between the cylinders, as illustrated in Fig. 1b. The incoming flow was aligned with this centerline, and the cylinders were positioned symmetrically above and below it.

### B. Cylinder Design

For the near-field surface pressure measurements, two circular cylinders with an outer diameter of $D = 22$ mm and a span length of $l = 460$ mm were used. To maintain the same diameter-based Reynolds number of $Re = 3.0 \times 10^4$ while accommodating the cylinders between the end plates, the dimensions were reduced to $D = 15.6$ mm and $l = 280$ mm for the acoustic measurements. The corresponding aspect ratios were approximately 21 and 18 for the near-field surface pressure and far-field noise experiments, respectively. Under these conditions, wall interference effects on the midspan flow were considered negligible [32]. Furthermore, according to Norberg [33], the spanwise coherence length $\Lambda$ for a single circular cylinder is approximately $3.2D - 4D$ at $Re = 3.0 \times 10^4$. Therefore, the aspect ratios employed in both setups were sufficient to ensure the development of a fully three-dimensional (3D) flowfield along the cylinder span. Therefore, by maintaining the same diameter-based Reynolds number and sufficiently large aspect ratios in both facilities, dynamically comparable flow conditions were ensured, such that the geometric scaling required by the different wind tunnels does not introduce significant differences in the wake development or the associated hydrodynamic–acoustic characteristics.

As shown in Fig. 2a, each cylinder used for the near-field surface pressure measurements consisted of three segments: a central section instrumented with static pressure taps and flush-mounted unsteady surface pressure transducers and two side sections extending the span to match the wind-tunnel width. In contrast, the cylinders used for the far-field noise measurements were manufactured as single, uniform pieces without segmented sections or instrumentation. As illustrated in Fig. 3, the central section of the near-field surface pressure cylinders was equipped with 18 static pressure ports, uniformly distributed around the circumference at a spanwise distance of $z = 72$ mm from the midspan. The angular spacing between taps was 20 deg. Each pressure tap had a diameter of 0.55 mm and was fitted with 5 mm long brass tubes, with inner and outer diameters of 0.4 and 0.6 mm, respectively. These brass tubes were connected to flexible polyurethane tubing, which routed the pressure signals to a multiport pressure scanner. Static pressure data were acquired using a 16-channel Honeywell electronic differential pressure measurement system, capable of measuring up to ±2.48 kPa with a system accuracy of ±2%. To ensure uniform coverage around the cylinder, the cylinders were rotated in 10 deg increments, allowing data collection at 36 distinct circumferential angles.

To measure unsteady surface pressure, the central section was instrumented with Panasonic WM-61A pressure transducers. Each sensor has a diameter of 6 mm, a height of 3.4 mm, and a 2 mm circular sensing area. These transducers, widely employed in previous studies [17–21,23,24,28,30], provide reliable measurements over a frequency range of 20 Hz to 10 kHz. For each cylinder, 15 transducers were installed to capture pressure fluctuations along both the spanwise and circumferential directions. The spanwise positions and circumferential angles of these transducers are listed in Table 1 for reference. Eight transducers ($p_1$–$p_8$) were placed nonuniformly along a $6D$ span using a potential function-based spacing to enable correlation analysis over various spanwise length scales. This configuration captures the 3D flow structures at the tested $Re$, in agreement with previous findings [33]. Because of

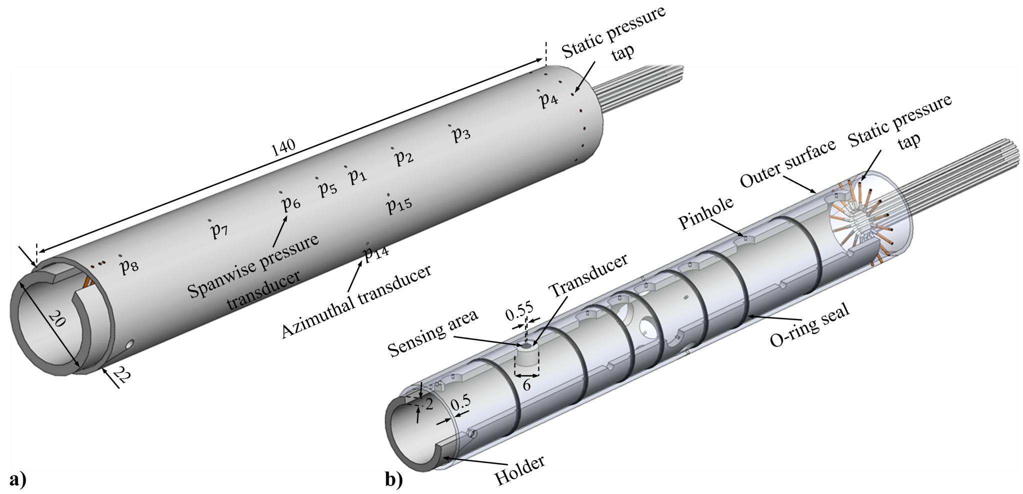


**Fig. 3 Schematic of the cylinder design a) middle section of the near-field surface pressure cylinders equipped with static pressure taps and unsteady pressure transducers and b) configuration of the flush-mounted unsteady pressure transducers beneath pinholes and arrangement of static pressure taps using the remote sensing method. Dimensions are given in millimeters.**

**Table 1 Summary of unsteady pressure transducer positions (note: $\theta$ is defined in Fig. 3a)**

| Transducer | $z/D$ | $\theta$, deg | Transducer | $z/D$ | $\theta$, deg |
|---|---|---|---|---|---|
| $p_1$ | 0.0 | 90 | $p_9$ | 0.282 | 45 |
| $p_2$ | 0.682 | 90 | $p_{10}$ | 0.0 | 0.0 |
| $p_3$ | 1.545 | 90 | $p_{11}$ | 0.282 | −45 |
| $p_4$ | 2.955 | 90 | $p_{12}$ | 0.0 | −90 |
| $p_5$ | −0.41 | 90 | $p_{13}$ | 0.282 | −135 |
| $p_6$ | −0.91 | 90 | $p_{14}$ | 0.0 | 180 |
| $p_7$ | −1.864 | 90 | $p_{15}$ | 0.282 | 135 |
| $p_8$ | −3.0 | 90 | — — | — — | — — |

spatial constraints, the remaining seven transducers ( $p_9$–$p_{15}$) were arranged circumferentially at two spanwise locations: $z = 0$ and $z \approx 6.2$ mm. At each location, four sensors were positioned at 90 deg intervals, resulting in an effective angular spacing of 45 deg between adjacent transducers.

To reduce attenuation effects at high frequencies, pressure measurements were conducted through small pinholes on the cylinder surface, as shown in Fig. 3b. Accurate dynamic pressure measurement at high frequencies is challenging due to spatial averaging when the wavelength of flow structures becomes smaller than the transducer's sensing area [30,34,35]. To address this, the transducers were mounted beneath 0.55 mm diameter pinholes and securely fixed inside the cylinder using a fully sealed holding mechanism. Although pinholes can potentially disturb the flow or introduce measurement errors at high frequencies, prior studies have shown that 0.55 mm pinholes do not significantly impact the boundary layer [34].

### C. Measurement Technique and Data Processing

To ensure measurement accuracy, all pressure transducers were calibrated before testing to correct for amplitude damping and phase delays introduced by the pinhole. Calibration was performed using a dedicated setup [30]. A 1/4 in. GRAS 40BP microphone, calibrated with a GRAS Sound Calibrator (Type 42AB), served as the reference. In situ calibration was conducted using white noise excitation over the frequency range of $f = 10$ Hz–20 kHz. The resulting transfer functions exhibited smooth, linear responses without resonances within the frequency range of interest (20 Hz–10 kHz) [30]. Power was supplied to the transducers via a 16-channel power module, and the data were acquired using a 16-channel National Instruments (NI) PCI-6023E data acquisition (DAQ) card at a sampling rate of 40 kHz over a 20 s period.

For the acoustic measurements, 16 ROGA MI-17 1/4-in. free-field microphones were used to record the acoustic signals, as shown in Fig. 2b. The microphones were positioned at a radial distance of 610 mm, pointing approximately at the midspan of the cylinders. The acoustic signals were acquired using a 24-bit NI DAQ card at a sampling frequency of 51.2 kHz over a 60 s duration. To convert the acquired pressure-time data into the frequency domain, a fast Fourier transform with Hanning windowing and 50% overlap was applied following Welch's method, resulting in a frequency resolution of 3.125 Hz. The resulting power spectral densities (PSDs) of the near- and far-field pressures, denoted as $\phi_{pp,s}$ and $\phi_{pp}$, respectively, are expressed in Pascals squared per Hertz, were then referenced to $p_0 = 20$ μPa to presented in decibels according to

$$\Phi_{pp} = 10\log_{10}\left(\frac{\phi_{pp}}{p_0^2}\right) \tag{1}$$

## III. Results and Discussion

### A. Acoustic Noise

Figure 4 presents the acoustic PSD, $\Phi_{pp}$ (decibels/hertz), measured at 90 deg relative to the flow direction, plotted as a function of the Strouhal number based on the cylinder diameter $St$. For the single-cylinder case, the emergence of the fundamental vortex-shedding tone, hereafter referred to as $f_1$ tone, with a magnitude $\Phi_{pp}|_{f_1}$ of approximately 76 dB is evident at $St \approx 0.2$ (see Fig. 4), which falls within the published $St$ range for $Re = 3.0 \times 10^4$ [33]. The $f_1$ tone is also referred to as the fundamental or first harmonic,

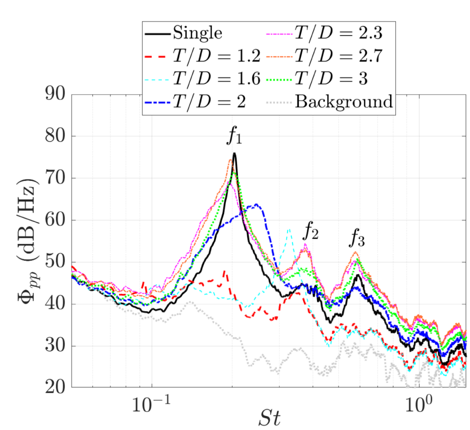


**Fig. 4 Acoustic PSD, $\Phi_{pp}$ (decibels/hertz), measured at 90 deg with respect to the flow direction (microphone 5 in Fig. 2a), plotted as a function of Strouhal number $St$.**

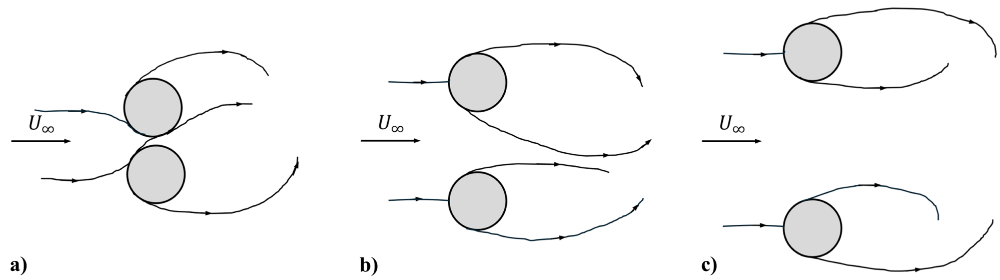


**Fig. 5 Schematic representation of flow patterns around side-by-side cylinders in cross-flow: a,b) biased gap flow patterns observed for 1.1–1.2 < $T/D$ < 2–2.2 and c) parallel vortex streets for $T/D$ > 2–2.2 [6].**

while tones at frequencies that are positive integer multiples of the fundamental frequency are termed higher harmonics [18,20]. It is observed that, in addition to the $f_1$ tone, the second and third harmonics, denoted as $f_2 = 2f_1$ and $f_3 = 3f_1$, respectively, also appear. However, their magnitudes, $\Phi_{pp}|_{f_2}$ and $\Phi_{pp}|_{f_3}$, are significantly smaller than that of the $f_1$ tone.

By switching to side-by-side cylinders, the tonal noises still appear, but their magnitudes and frequencies differ from those of the single cylinder, except at $T/D = 3$. This behavior arises from differences in the governing flow regimes and wake characteristics. At $T/D = 1.2$, the wake behind the cylinders becomes highly unsteady and asymmetric, indicating the dominance of the biased-gap flow (BGF) regime [3,6,36,37]. In this regime, as described by Alam et al. [38], the gap flow deflects toward one cylinder, leading to distinct wake structures behind each body. The cylinder toward which the flow is biased develops a narrower wake and sheds vortices at a higher frequency (mode NW in the present study), as shown in Fig. 5a, whereas the other cylinder forms a wider wake with lower-frequency vortex shedding (mode WW). Consequently, mode NW induces higher drag, while mode WW corresponds to lower drag on their respective cylinders [36,39]. As illustrated in Fig. 4, these distinct wake modes manifest acoustically as two dominant tones at $St \approx 0.09$ and $St \approx 0.34$, which occur at higher and lower frequencies, respectively, than that of the $f_1$ tone. This behavior reflects the asymmetric vortex-shedding characteristics inherent to the BGF regime and is consistent with previous experimental observations [9,36,37,40,41]. In addition to these tones, an intermediate tone appears at $St \approx 0.19$, which is close to the $f_1$-tone frequency. This observation agrees with the findings of Alam et al., who identified an additional flow mode corresponding to this intermediate tone. It is evident that the magnitudes of all these tones are substantially reduced compared to those of the single cylinder. This reduction demonstrates that the side-by-side configuration effectively suppresses tonal noise generation through mutual aerodynamic interference and altered vortex-shedding dynamics. However, this suppression capability gradually diminishes as the spacing ratio increases, and the flow progressively approaches the behavior of a single cylinder.

It is observed that increasing the spacing ratio from $T/D = 1.2$ causes both the low- and high-frequency tones to shift closer to the $f_1$-tone frequency. In addition, while the low-frequency tone decreases in magnitude, the high-frequency tone increases substantially. This trend leads to the emergence of a single dominant tone at $T/D = 2$, with a magnitude of approximately 63 dB, still about 13 dB lower than the single-cylinder case, located at $St \approx 0.25$. Although the BGF regime persists at this spacing and the gap flow remains weakly biased, as shown in Fig. 5b and discussed by Sumner [6] and Alam et al. [38], the previously distinct low- and high-frequency modes merge into a single synchronized vortex-shedding frequency. This behavior demonstrates that frequency synchronization can occur even when the wakes remain asymmetric [38,42].

By further increasing the spacing ratio to $T/D = 3$, the tonal noise becomes nearly identical to that of the single cylinder in both magnitude and Strouhal number. This behavior indicates that the wakes behind the two cylinders become similar and that vortex shedding occurs at the same frequency for both bodies. This flow regime, known as the parallel vortex-shedding (PVS) regime [6], is characterized by synchronized vortex shedding occurring in either in-phase or antiphase modes [43,44]. However, most studies report that although both synchronization modes are possible, antiphase shedding typically dominates [36,41,45,46], as illustrated in Fig. 5c.

The spectrograms obtained from the short-time Fourier transform (STFT), shown in Fig. 6, illustrate the tonal noise behavior of selected side-by-side configurations in comparison with the single-cylinder case. In particular, for $T/D = 1.2$, low- and high-frequency tones, along with an intermediate tone (all relative to the $f_1$-tone frequency of the single cylinder or $T/D = 3$; see Figs. 6a and 6d), persist over most of the time domain (Fig. 6b). For $T/D = 2$, a single high-frequency tone dominates throughout the time range. Although the STFT provides a general overview of the frequency content, its fixed time-frequency resolution limits the ability to resolve rapid switching between multiple coexisting tones, particularly for $T/D = 1.2$. To overcome this limitation, the real part of the wavelet transform $\Re\{W\}$ using the Morlet mother wavelet [24], is presented in Fig. 7 over a short time interval. Unlike STFT, the wavelet transform offers adaptive time-frequency resolution, enabling simultaneous identification of multiple frequencies and their temporal evolution. It is evident that the single cylinder and the side-by-side configuration at $T/D = 3$ (Figs. 7a and 7d, respectively) exhibit repeatable single-frequency patterns, whereas

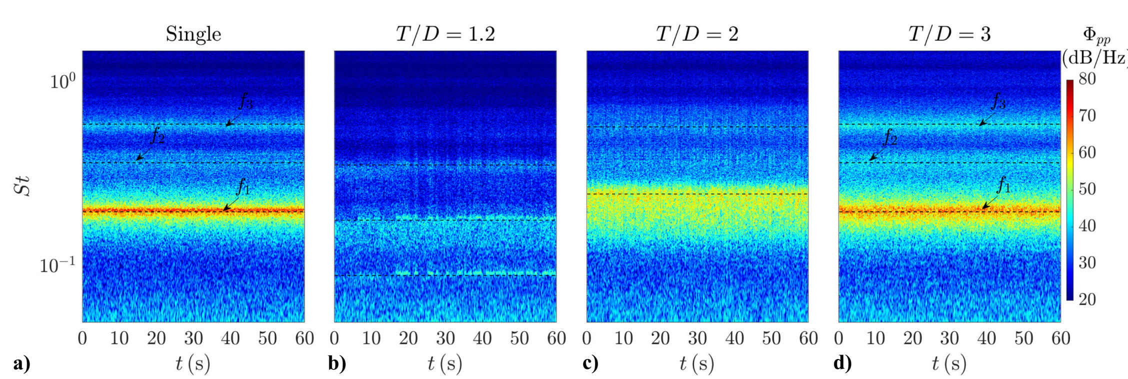


**Fig. 6 Spectrograms of the far-field acoustic signal of microphone 5 for the single cylinder and side-by-side cylinder configurations.**

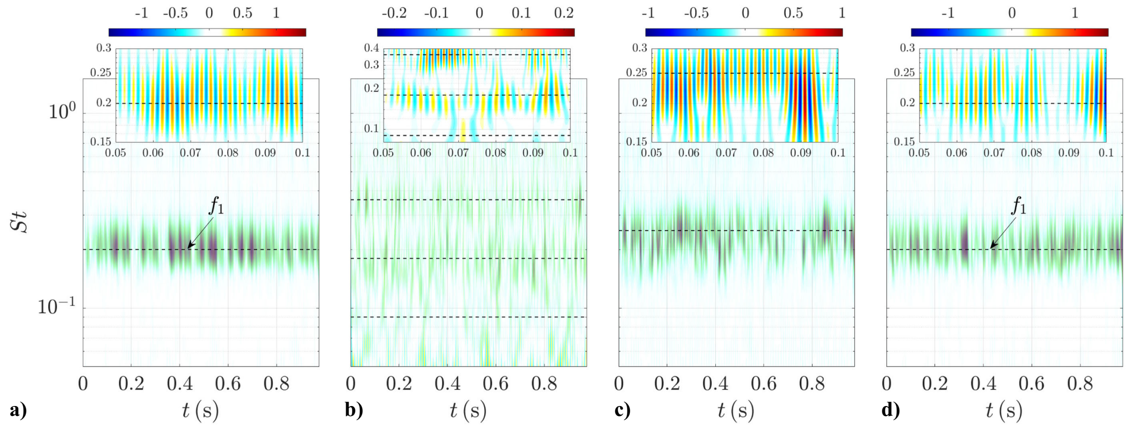


**Fig. 7 Real part of the wavelet transform $\Re\{W\}$ of the far-field acoustic signal of microphone 5 for a) single cylinder and b–d) side-by-side configurations at $T/D = 1.2$, 2, and 3, respectively. Different color bar ranges were chosen to clearly highlight the repeatable patches and temporal evolution of dominant frequencies for each case.**

the $T/D = 1.2$ case shows alternating energy among three frequencies, highlighting the highly unsteady and biased vortex shedding (Fig. 7b). A weaker form of this behavior appears at $T/D = 2$, but it is far less pronounced than at $T/D = 1.2$ as illustrated in Fig. 7c.

To investigate the acoustic directivity, the variations of $\Phi_{pp}$ at the dominant tonal frequencies and the overall sound pressure level (OASPL, in decibels) at all tested polar angles (see Fig. 3b) are presented in Fig. 8. The OASPL was computed over the frequency range corresponding to $St \approx 0.8$–2 as

$$\mathrm{OASPL} = 10\log_{10}\left(\frac{\int \Phi_{pp}\,\mathrm{d}f}{p_0^2}\right)\ \mathrm{dB} \tag{2}$$

The distribution of both the dominant tonal magnitude and the OASPL for the single-cylinder case exhibits two symmetric arcs on either side of the cylinder relative to the flow direction. Although the available data points are insufficient to fully resolve the acoustic directivity pattern, these lobelike features, consistent with the findings of Gloerfelt et al. [47] and Inoue and Hatakeyama [48], provide evidence of dipolelike acoustic radiation oriented perpendicular to the incoming flow.

Using the single-cylinder case as a reference for dipolelike radiation, the directivity patterns of the side-by-side configurations can be interpreted based on their similarity to the single-cylinder behavior. For smaller spacing ratios ($T/D = 1.2$ and 1.6), a simple dipolelike pattern is recovered only in the OASPL distribution (Fig. 8b), whereas the directivity of the dominant tonal magnitude departs from that of the single cylinder and becomes asymmetric with respect to the flow direction (Fig. 8a). This asymmetry is attributed to the BGF, which induces persistent wake asymmetry and causes the dominant tonal radiation to depend on the prevailing shedding mode (NW, WW, or intermediate). In contrast, for larger spacing ratios, particularly for $T/D \gtrsim 2$–3, the directivity patterns of both the dominant tonal magnitude and the OASPL closely resemble those of the single cylinder, indicating recovery of dipolelike acoustic radiation. These observations indicate that, while the dominant tonal radiation can be strongly asymmetric at small spacings due to mode-dependent wake dynamics, the frequency-integrated acoustic field, combining tonal and broadband contributions, retains an approximately dipolelike radiation pattern.

### B. Near-Field Surface Pressure Characteristics

#### *1. Steady Near-Field Surface Pressure*

Figures 9a and 9b present the mean static pressure coefficient $C_p$ distributions for the lower and upper cylinders, respectively. For the single-cylinder case, $C_p$ reaches a maximum near 1 at the front stagnation point $\theta_{fs}$ within the region of favorable pressure gradient and then decreases rapidly to a minimum at $\theta_m \approx 62$ deg. As the flow enters the adverse pressure gradient region, $C_p$ gradually rises (i.e., becomes less negative), signaling the approach of boundary layer separation. This increase continues until $\theta_b \approx 85$ deg, which defines the onset of the base region. Within this base region,

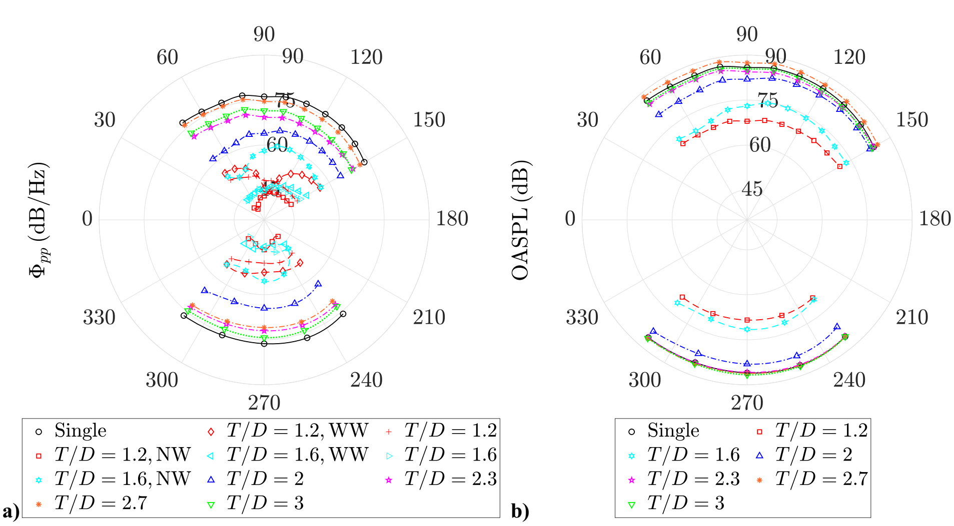


**Fig. 8 Directivity patterns of a) $\Phi_{pp}$ at the dominant tonal frequencies (corresponding, for $T/D = 1.2$ and 1.6, to the low- and high-frequency tones associated with the WW and NW modes, respectively, as well as the intermediate tone) and b) the OASPL (decibels). The flow direction is from left to right.**

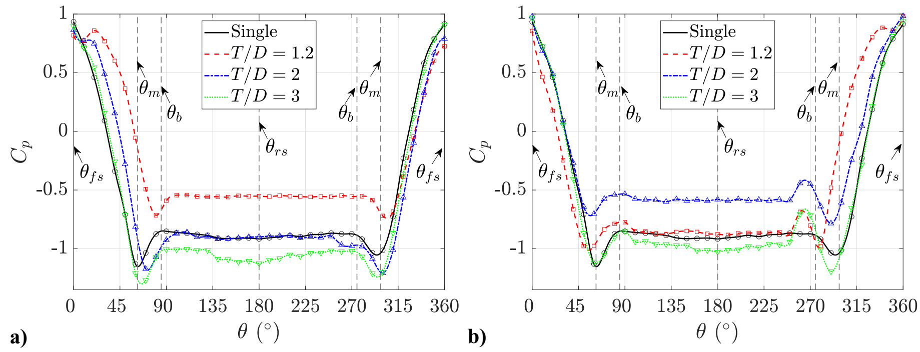


**Fig. 9 Mean pressure coefficients $C_p$ around the circumference of the side-by-side cylinders: a) lower cylinder and b) upper cylinder. For reference, in the single-cylinder case, the front and rear stagnation points ($\theta_{fs}$ and $\theta_{rs}$) occur at $\theta = 0$ and 180 deg, respectively. The angular locations where $C_p$ reaches its minimum and where the base region begins are denoted by $\theta_m$ and $\theta_b$, respectively.**



$C_p$ remains nearly constant, exhibiting a deviation of only about 3% between $\theta_b$ and the rear stagnation point $\theta_{rs}$ in agreement with prior studies [49,50]. At the investigated Reynolds number of $Re = 3.0 \times 10^4$, the flow lies within the subcritical regime, characterized by laminar separation followed by the formation of turbulent vortices in the cylinder wake [51]. In this regime, the pressure distribution on the upper and lower surfaces of a single cylinder is essentially symmetric [49,52,53], reflecting the uniform development of the boundary layer around the cylinder.

Although the circumferential variation of $C_p$ for both the lower and upper cylinders in the side-by-side configurations generally follows the trend observed for a single cylinder, notable deviations arise at small spacing ratios. Specifically, at $T/D = 1.2$, the lower cylinder exhibits a forward shift of $\theta_{fs}$ and $\theta_m$ to approximately 20 and 80 deg, respectively, as shown in Fig. 9a. Owing to the geometric symmetry of the configuration, the corresponding positions for the upper cylinder shift to $\theta_{fs} = 340$ deg and $\theta_m \approx 280$ deg, as depicted in Fig. 9b. This pressure distribution is consistent with the BGF characteristics reported by Alam and Zhou [54] for the same spacing. At this $T/D$ ratio, although the lower and upper cylinders exhibit symmetric behavior before flow separation, particularly in terms of $\theta_{fs}$ and $\theta_m$, the shear layers develop differently due to the gap flow imposing an asymmetric influence on the two cylinders. This asymmetry is particularly evident in the base region: for the lower cylinder, this region begins near $\theta_b \approx 100$ deg and stabilizes around $C_p = -0.55$ (Fig. 9a), whereas for the upper cylinder, it starts at $\theta_b \approx 252$ deg and decreases further to approximately $C_p = -0.85$, indicating weaker pressure recovery (Fig. 9b). The difference in base pressure reflects potentially lower drag on the lower cylinder, resulting from the gap flow being biased toward the upper cylinder. According to Alam and Zhou, after separating from the top surface of the lower cylinder, the gap flow impinges on the bottom side of the upper cylinder, sweeps around it, and proceeds downstream before detaching from its rear surface, as illustrated in Fig. 5a. This redistribution of the gap flow reduces the momentum exchange and entrainment in the wake of the lower cylinder, leading to a relatively higher (less negative) base pressure and thus lower pressure drag, despite the geometrically wider wake (mode WW). This behavior contrasts with that of an isolated cylinder, where a broader wake is typically associated with lower base pressure and increased drag. In the biased side-by-side configuration, however, wake width is governed by the gap-flow deflection mechanism rather than by the classical pressure-recovery behavior of a single bluff body.

By increasing $T/D$ to 2, where the BGF regime still prevails, $\theta_{fs}$ and $\theta_m$ for both the lower and upper cylinders tend to approach those of a single cylinder. This behavior can be attributed to the gap distance at this $T/D$, which equals the cylinder diameter; hence, direct impingement of the separated shear layer from the bottom of one cylinder onto the top of the other is uncommon, as noted by Alam and Zhou [54]. Nevertheless, the gap flow remains preferentially deflected due to the BGF characteristics. This is further confirmed by the base-region pressure coefficient, which stabilizes at approximately $C_p = -0.85$ for the lower cylinder (Fig. 9a) and recovers to about $C_p = -0.55$ for the upper cylinder (Fig. 9b), indicating a deflection of the gap flow toward the lower cylinder (Fig. 5b) and resulting in a narrower wake behind it compared to the upper cylinder.

At a further increased spacing ratio of $T/D = 3$, the $C_p$ distribution for both the upper and lower cylinders closely resembles that of a single cylinder. This behavior is characteristic of the PVS regime, where the flowfield regains its symmetry and both cylinders undergo von-Kármán vortex shedding at the same frequency as illustrated in Fig. 5c. In this regime, the two side-by-side cylinders behave more like independent, single cylinders [6].

### 2. *Unsteady Near-Field Surface Pressure*

The near-field surface pressure PSD $\Phi_{pp,s}$ (decibels/hertz) as a function of $St$, is presented in Figs. 10 and 11 for the lower and upper cylinders, respectively. For the single-cylinder case, a distinct peak appears at $St \approx 0.2$ across nearly all circumferential angles, except at $\theta = \theta_{rs} = 180$ deg. This peak corresponds to the $f_1$ tone in Fig. 4, confirming that the dominant surface pressure fluctuations originate from vortex shedding [17–24,28,30,48,55,56] and are closely correlated with far-field acoustic radiation [17–21]. It should be noted that far-field noise arises from both quadrupolelike acoustic radiation generated in the wake, where vortex shedding occurs, and dipolelike radiation scattered from the cylinder surface due to pressure fluctuations originating from shear-layer interactions and rapid vertical flow motions within the vortex formation region [47]. However, the latter contribution is more dominant [18,20], consistent with the classical understanding that, at low Mach numbers, dipole sources govern far-field noise generation, whereas quadrupole sources play a secondary role [57]. Apart from the $f_1$ peak, the second and third harmonics, corresponding to the $f_2$- and $f_3$-peak frequencies, respectively, are observed within $\theta = 45$–135 deg and $\theta = 225$–312 deg, corresponding to the shoulder regions on the top and bottom sides of the cylinder. Alternating pressure fluctuations in these shoulder regions, particularly at the $f_1$- and $f_3$-tone frequencies, act as the primary sources of lift fluctuations [17–19,23,28,33,56]. In contrast, pressure fluctuations outside these regions, particularly near $\theta_{fs}$ and, more prominently, $\theta_{rs}$, primarily contribute to drag fluctuations. This explains why, at $\theta = 180$ deg, the $\Phi_{pp,s}$ spectrum at the $f_1$-tone frequency appears entirely broadband, with no distinct peak. Instead, the dominant peak emerges at the $f_2$-peak frequency, consistent with previous observations [17–21,23,24,30].

By examining Figs. 10 and 11 for the side-by-side configurations, the emergence of peaks corresponding to the tonal noise observed in Fig. 4 is evident for both the lower and upper cylinders, indicating that the underlying noise generation mechanism remains consistent with that of the single cylinder. However, except at $T/D = 3$, these peaks deviate from those of the single cylinder in both magnitude and Strouhal number. For instance, at $T/D = 1.2$, the magnitudes of both the low- and high-frequency peaks (relative to the $f_1$ peak)

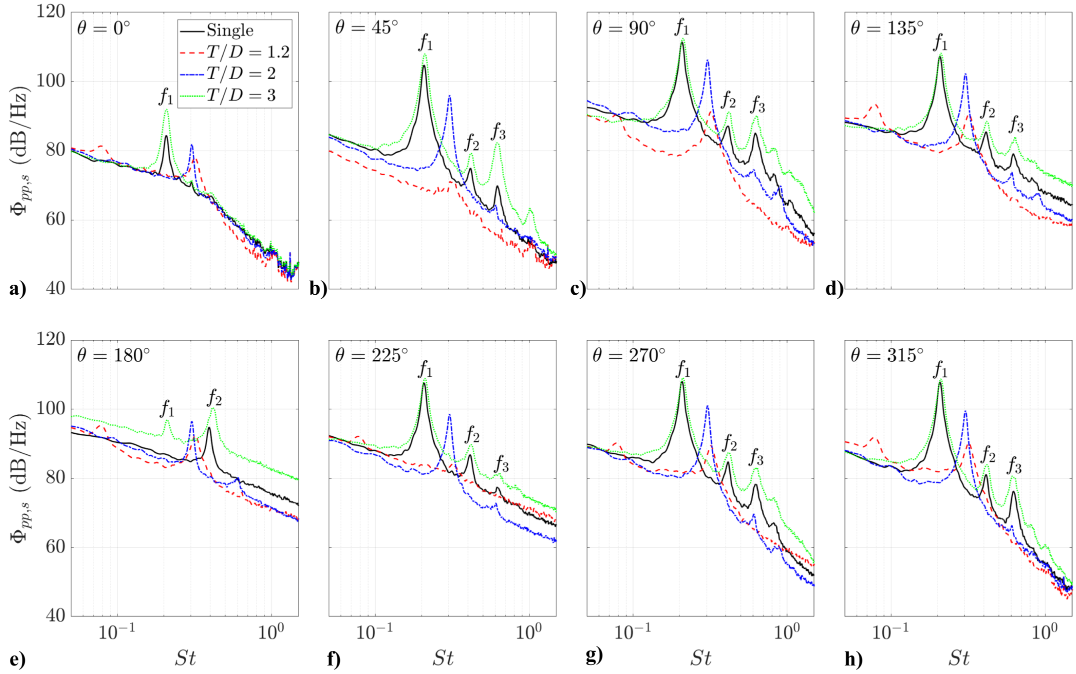


**Fig. 10** **PSD of near-field surface pressure $\Phi_{pp,s}$ (decibels/hertz), around the circumference of the lower cylinder as a function of *St*.**

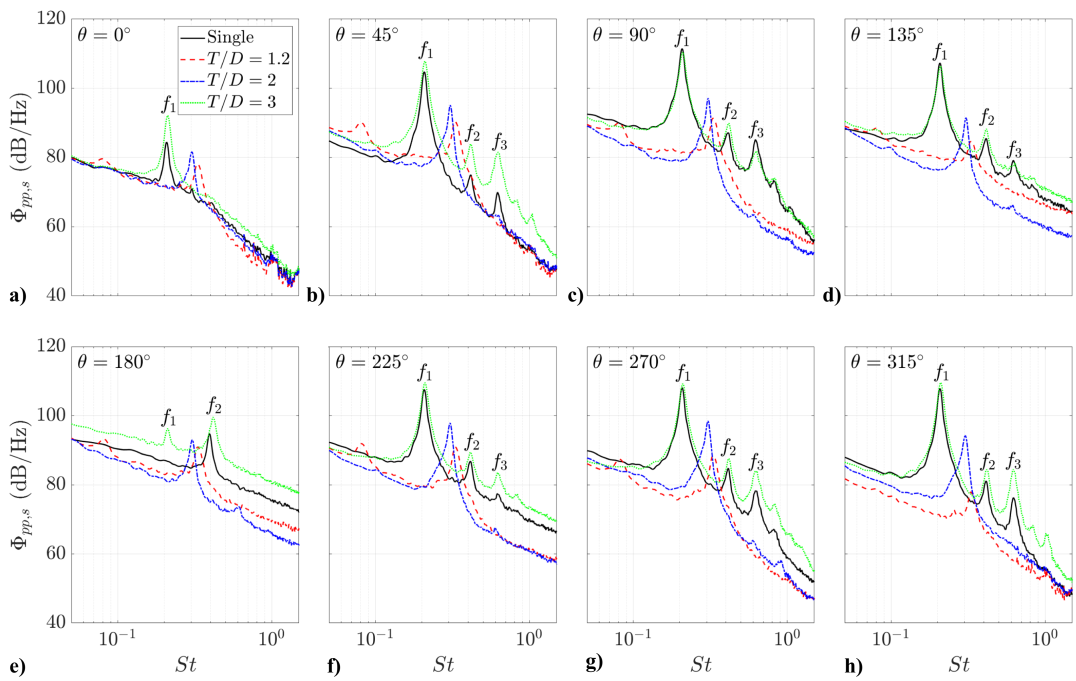


**Fig. 11** **PSD of near-field surface pressure $\Phi_{pp,s}$ (decibels/hertz), around the circumference of the upper cylinder as a function of *St*.**

decrease compared with the single-cylinder case, with a more pronounced reduction for the low-frequency peak, particularly at $\theta = 45$ and 315 deg for the lower and upper cylinders, respectively, as shown in Figs. 10b and 11h. Although these angles do not coincide with $\theta_{fs}$ identified for this spacing in Fig. 9, they provide evidence of gap-flow deflection from the upper side of the lower cylinder toward the lower side of the upper cylinder. Apart from $T/D = 1.2$, a reduction in peak magnitude occurs at $T/D = 2$, although it is less significant than that observed at $T/D = 1.2$. Considering the dominant contribution of surface pressure fluctuations to far-field noise, this attenuation of surface pressure fluctuations is identified as the primary mechanism responsible for the noise reduction observed in Fig. 4.

It is worth noting that, in addition to differences in magnitude and frequency, the circumferential distribution of the dominant peak around both the lower and upper cylinders, particularly at $T/D = 1.2$, also deviates from that observed for the single cylinder. To highlight these differences, the directivity of the dominant peak is illustrated in Fig. 12. As the directivity patterns of the low- and high-frequency peaks at $T/D = 1.2$ are similar, only the latter is presented here for clarity. It is evident that the dominant peak magnitude on the top side of the single cylinder increases from $\theta = 0$ deg, reaches a maximum around $\theta = 90$ deg, and gradually decreases to vanish at $\theta = 180$ deg (see Figs. 10 and 11). A symmetric behavior is observed approximately on the bottom side, resulting in a dipolelike directivity pattern oriented perpendicular to

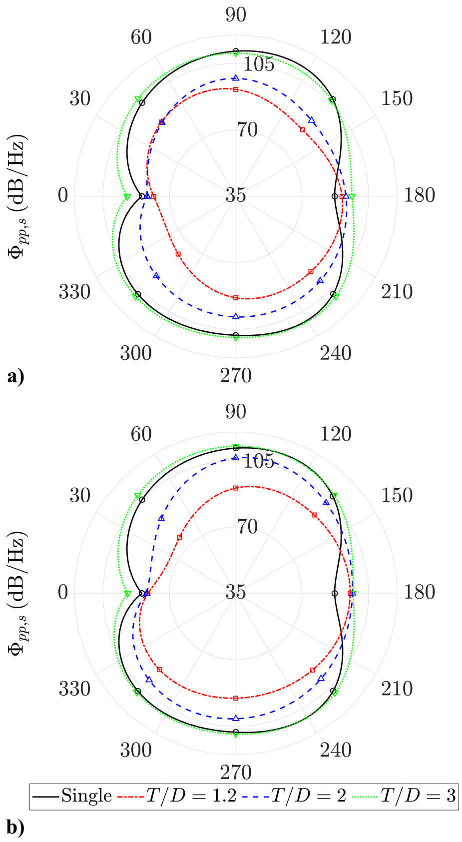


**Fig. 12 Directivity of $\Phi_{pp,s}$ at the dominant peak frequency (corresponding to the high-frequency peak for $T/D = 1.2$): a) upper cylinder and b) lower cylinder. The flow direction is from left to right.**

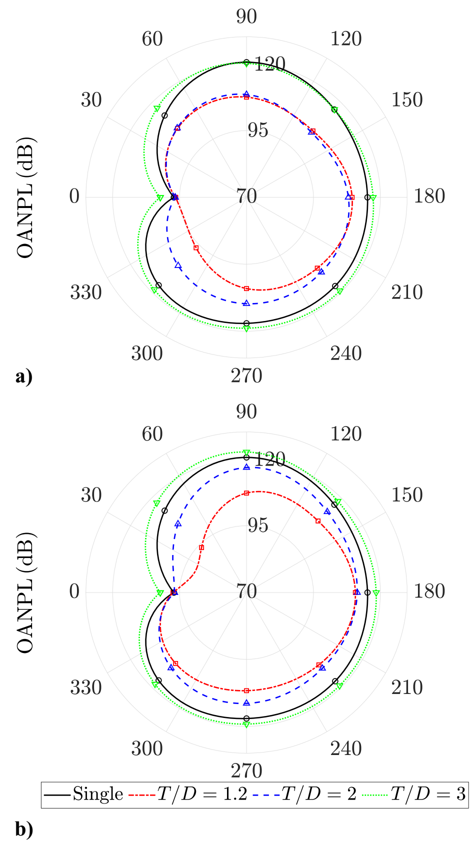


**Fig. 13 Directivity of the OANPL (decibels) for a) the upper cylinder and b) the lower cylinder. The flow direction is from left to right.**

the flow, consistent with previous studies [17,20,23,24,28]. This pattern, in line with the observations in Fig. 8a, supports the correlation of surface pressure fluctuations with acoustic waves scattered from the cylinder surface to the far field at the $f_1$-tone frequency [17,20,24,47].

For the side-by-side cylinders, the dipolelike directivity pattern of the peak magnitude is largely restored at $T/D = 3$, although the typical indentation at $\theta = 180$ deg is absent. This suggests that the gap flow no longer significantly influences the cylinder surface, and the vortex shedding behavior closely resembles that of an isolated cylinder. For smaller spacing ratios, particularly $T/D = 1.2$, an elliptic directivity pattern emerges, with its major axis connecting the locations of maximum magnitude of the dominant peak at $\theta = 45$ and 225 deg for the upper cylinder (Fig. 12a) and at $\theta = 135$ and 315 deg for the lower cylinder (Fig. 12b), tilted clockwise and counterclockwise, respectively. Assuming that near-to-far-field correlation persists for the side-by-side configuration particularly at this spacing ratio, the observed elliptic directivity supports the nondipolelike radiation pattern identified in Fig. 8a and the presence of the BGF regime.

At $T/D = 2$, the peak magnitude around the upper and lower cylinders exhibits an approximately semi-dipole-like directivity pattern perpendicular to the flow. However, the upper and lower lobes of this pattern are asymmetric compared to the single-cylinder case. Notably, the dominant peak magnitude on the bottom side of the upper cylinder appears larger than on its top side, while the opposite trend is observed for the lower cylinder. This behavior indicates a deflection of the gap flow toward the top side of the lower cylinder.

From Figs. 10 and 11, it is evident that, in addition to differences in the magnitude of the dominant peak, the side-by-side cylinders, particularly at $T/D = 1.2$ and 2, exhibit distinct broadband surface pressure fluctuations compared to the single-cylinder case. To further examine this discrepancy, the overall near-field surface pressure level (OANPL, decibels) was calculated over the entire frequency range of interest using Eq. (2) and the resulting directivity patterns are shown in Fig. 13. It is observed that the OANPL directivity around the circumference of all cylinders, except at $\theta = 180$ deg, particularly for the single-cylinder case, closely resembles that of the dominant peak magnitude shown in Fig. 12. This similarity indicates that surface pressure fluctuations at the dominant peak frequency contribute most significantly to the OANPL, compared to fluctuations at other frequencies. This further explains why, for bluff bodies, the majority of far-field noise scattered from the surface occurs at the dominant peak frequency. Despite this, the influence of broadband surface pressure fluctuations cannot be neglected, as they contribute to amplifying the OANPL beyond the magnitude of the dominant peak for all cylinders. At $T/D = 1.2$ and 2, the OANPL is smaller in magnitude than at $T/D = 3$, where it closely matches that of the single cylinder across nearly all angles. For $T/D = 1.2$ and 2, the OANPL remains generally comparable in magnitude on the top side of the upper cylinder (Fig. 13a) and the bottom side of the lower cylinder (Fig. 13b). The only notable discrepancy between these two spacings appears on the upstream side of the gap region, where the side-by-side cylinders at $T/D = 1.2$ exhibit smaller OANPL than those at $T/D = 2$, specifically within $\theta = 270$–360 deg for the upper cylinder and $\theta = 0$–90 deg for the lower cylinder. This behavior further supports the contribution of broadband surface pressure fluctuations to the OANPL.

### C. Lift and Drag Characteristics

#### *1. Mean Drag Coefficient*

As shown in Fig. 9, the asymmetric distribution of $C_p$ in the base region between the lower and upper cylinders indicates the formation of wakes with different widths, most prominently at $T/D = 1.2$. This asymmetry, further supported by the observations in Figs. 12 and 13, implies corresponding differences in drag between the two cylinders. Although drag was not directly measured in this study, additional insight was obtained by integrating $C_p$ from Fig. 9 around the cylinder to estimate the drag coefficient $C_d$

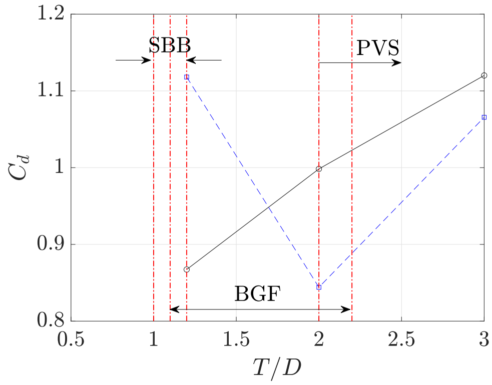


**Fig. 14 Variation of mean drag coefficient $C_d$ as a function of $T/D$. Black solid and blue dashed lines represent the lower and upper cylinders, respectively. Based on the gap flow behavior: single-bluff-body (SBB) behavior for $1 < T/D < 1.1$–$1.2$, BGF for $1.1$–$1.2 < T/D < 2$–$2.2$, and PVS for $T/D > 2$–$2.2$ [6].**

following the approach of Maryami and Liu [20], whose variation with $T/D$ is presented in Fig. 14.

At $T/D = 1.2$, the lower cylinder exhibits a smaller $C_d$ than the upper cylinder, supporting the earlier inference that the lower cylinder develops a wider wake region than the upper one (see Fig. 5a). Moreover, compared to the single-cylinder case ($C_d \approx 1.02$ [58,59]), the lower cylinder shows a reduced $C_d$, while the upper cylinder exhibits an increased $C_d$; these discrepancies also reflect a corresponding difference in wake characteristics between the single-cylinder and side-by-side configuration, highlighting the impact of cylinder interaction on the flow structure. As the spacing increases to $T/D = 2$, the lower cylinder exhibits a higher $C_d$ than the upper cylinder, reversing the trend observed at $T/D = 1.2$ and consistent with the expected wake characteristics of the cylinders (see Fig. 5b). However, relative to the single-cylinder case, this trend is not entirely opposite to that at $T/D = 1.2$; the upper cylinder shows a reduction in $C_d$, while the lower cylinder's $C_d$ remains close to that of the single cylinder. At $T/D = 3$, where both cylinders are expected to exhibit wake behavior similar to that of a single cylinder (see Fig. 5c), the $C_d$ of the upper and lower cylinders converge and are higher than that of the single cylinder. This increase likely arises from residual mutual interference, weak shear-layer interactions, and flow disturbances induced by the neighboring cylinder.

### 2. *Unsteady Lift and Drag Coefficient*

To gain further insight into the aerodynamic force behavior of side-by-side cylinders, the PSD of the unsteady lift and drag coefficients, $\phi_{C_lC_l}$ and $\phi_{C_dC_d}$ (1/Hz), respectively, is presented in Fig. 15, following the method outlined in previous studies [19,24]. The unsteady lift and drag forces were obtained by integrating the unsteady surface pressure around the entire circumference of each cylinder [33]. It is worth noting that within the subcritical Reynolds number regime, the contribution of skin friction to total drag is negligible, typically less than 2% [49]. Therefore, skin friction was excluded from the drag estimation.

From Fig. 15, it is observed that, for the single-cylinder case, the $\phi_{C_lC_l}$ and $\phi_{C_dC_d}$ spectra exhibit dominant peaks at the $f_1$- and $f_2$-peak frequencies, respectively, consistent with previous studies [17–19,23,24,28,56,60]. The higher magnitude of the $f_1$ peak highlights the predominance of lift fluctuations induced by periodic vortex shedding, which drives flow-induced noise [33]. The dominant peak in $\phi_{C_lC_l}$ coincides with that of $\Phi_{pp,s}$ at $\theta = 90$ and 270 deg (Figs. 10c and 10g), whereas the dominant peak in $\phi_{C_dC_d}$ aligns with that at $\theta = 180$ deg (Fig. 10d), confirming that lift fluctuations are primarily driven by surface pressures away from the base, while drag fluctuations are dominated by base pressure.

In terms of the dominant peaks in the $\phi_{C_lC_l}$ and $\phi_{C_dC_d}$ spectra, the side-by-side cylinders generally exhibit similar behavior to the single cylinder, except at $T/D = 1.2$. At this spacing, although both low- and high-frequency peaks are evident in the $\phi_{C_lC_l}$ spectrum of the lower cylinder (Fig. 15a), the high-frequency peak and its second harmonic appear in the $\phi_{C_dC_d}$ spectrum. Similar behavior is observed for the upper cylinder; however, the low-frequency peak disappears entirely, and the high-frequency peak becomes dominant, as shown in Fig. 15c.

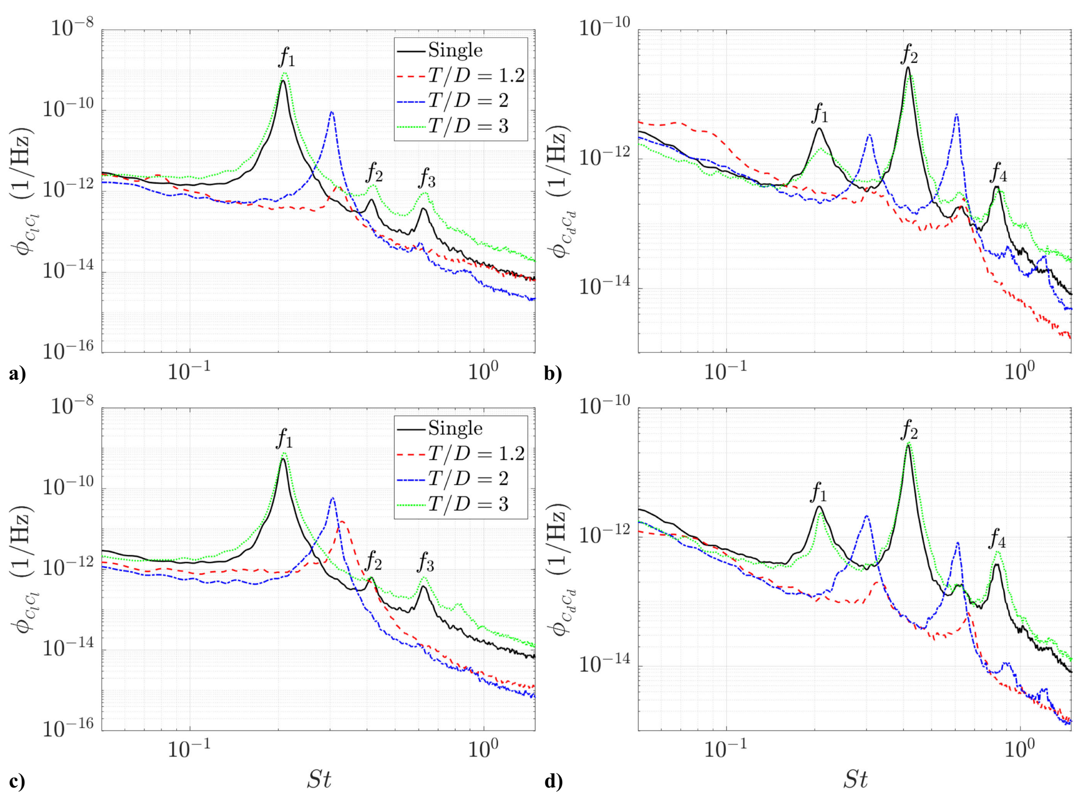


**Fig. 15 PSD of the aerodynamic force coefficients: a,c) PSD of the lift coefficient $\phi_{C_lC_l}$ (1/Hz) and b,d) PSD of the drag coefficient $\phi_{C_dC_d}$ (1/Hz) as functions of $St$. Here a and b correspond to the lower cylinder, and c and d correspond to the upper cylinder.**

It is observed that, except at $T/D = 3$, where the magnitudes of the dominant peaks closely match those of the single cylinder, the peak magnitudes at $T/D = 1.2$ and 2 are reduced, with the most pronounced reduction occurring at $T/D = 1.2$. Given the well-established correlation between lift fluctuations and far-field noise, the attenuation of the dominant peaks in the $\phi_{C_lC_l}$ spectra at these spacings further supports the observed reduction in far-field noise shown in Fig. 4. Apart from the differences between the single-cylinder and side-by-side configurations, discrepancies also arise between the lower and upper cylinders in terms of dominant peak magnitudes. As shown in Figs. 15a and 15c, at $T/D = 1.2$, the dominant (high-frequency) peak in the $\phi_{C_lC_l}$ spectrum of the lower cylinder is smaller than that of the upper cylinder, whereas this trend reverses at $T/D = 2$. In contrast, the $\phi_{C_dC_d}$ spectra in Figs. 15b and 15d reveal that the dominant peak magnitude of the lower cylinder exceeds that of the upper cylinder at both spacings. The behavior observed at $T/D = 1.2$ deviates from the $C_d$ trends in Fig. 14, suggesting that the unsteady wake dynamics and mutual interference between the two cylinders induce asymmetric vortex shedding and fluctuating loading that are not fully reflected in the time-averaged drag coefficient.

### D. Spanwise Coherence

Evaluating the spanwise extent over which the flow remains two dimensional (2D) is essential, as it influences both the scattering of acoustic waves from the surface of the cylinders and the propagation of acoustic waves generated in the wake region to the far field. To provide further insight into this aspect, the magnitude-squared coherence of the near-field surface pressure fluctuations, denoted as $\gamma^2_{p_ip_j,s}$, is calculated. This quantity measures the frequency-dependent correlation between a reference pressure signal (subscript $i$) and another pressure signal (subscript $j$) and is defined as

$$\gamma^2_{p_ip_j,s} = \frac{|\phi_{p_ip_j,s}(f)|^2}{\phi_{p_ip_i,s}(f)\phi_{p_jp_j,s}(f)} \tag{3}$$

where $\phi_{p_ip_j,s}$ is the cross-spectrum between the two signals and $\phi_{p_ip_i,s}$ and $\phi_{p_jp_j,s}$ are the auto-spectra of signals $i$ and $j$, respectively.

Although there are 28 unique spanwise spacings, $\Delta z = \eta$, Figs. 16 and 17 present $\gamma^2_{p_ip_j,s}$ as a function of $St$ for the lower and upper cylinders, respectively, for selected values of $\eta/D$ spanning the full range from minimum to maximum. For the single cylinder, at $\eta/D = 0.41$, the spanwise coherence of surface pressure fluctuations at the $f_1$-peak frequency $\gamma^2_{p_ip_j,s}|_{f_1}$ remains close to unity, indicating strong two-dimensionality resulting from correlated vortex shedding along the span. As $\eta/D$ increases, $\gamma^2_{p_ip_j,s}|_{f_1}$ gradually decreases, falling mostly below 0.5 beyond $\eta/D = 3.41$. A similar trend is observed for $\gamma^2_{p_ip_j,s}$ at the dominant-peak frequency in the side-by-side configurations, except at $T/D = 1.2$, where the coherence drops below 0.5 much earlier, beyond $\eta/D = 0.68$. This behavior, consistent with the observations in Figs. 4, 10, and 11, suggests that when the flow remains 2D over a shorter spanwise extent, the resulting attenuation of near-field surface pressure fluctuations leads to a greater reduction in far-field noise.

For further analysis, Fig. 18 presents $\gamma^2_{p_ip_j,s}$ at the dominant-peak frequency across all $\eta/D$. It is evident that, for all cases, this $\gamma^2_{p_ip_j,s}$ decays exponentially with increasing $\eta/D$. As shown in Fig. 18a, the lower cylinder exhibits a decay pattern generally similar to that of the single cylinder across all side-by-side configurations, except at $T/D = 1.2$, where a noticeably faster decay occurs. This is evident from the spanwise location at which $\gamma^2_{p_ip_j,s}$ drops below 0.5, approximately at $\eta/D = 1.86$ for $T/D = 1.2$, compared to $\eta/D = 3.1$ for the other cases. For the upper cylinder (Fig. 18b), the decay at $T/D = 1.2$ remains the fastest and is slightly more pronounced than that of the lower cylinder, with $\gamma^2_{p_ip_j,s}$ dropping below 0.5 at $\eta/D \approx 1.6$. As $T/D$ increases, the decay rate decreases; at $T/D = 2$, where $\gamma^2_{p_ip_j,s}$ falls below 0.5 beyond $\eta/D \approx 4$, it becomes slower than that of the single cylinder. Although the decay rate increases again at $T/D = 3$, approaching the single-cylinder trend, it remains lower than the rate observed at $T/D = 1.2$.

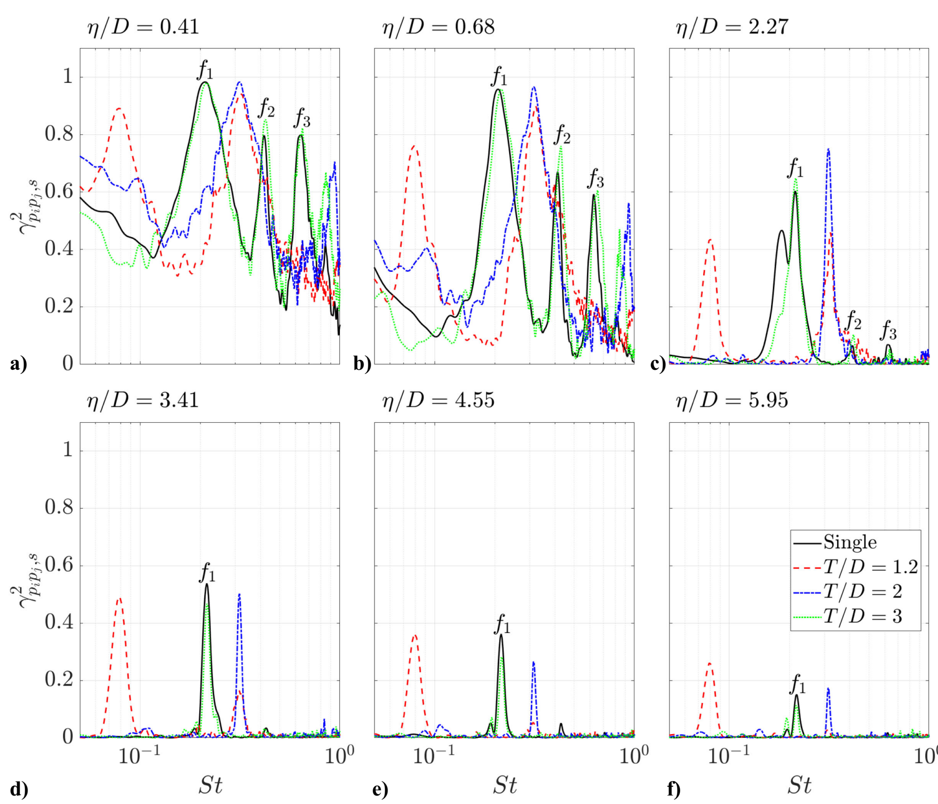


**Fig. 16 Spanwise coherence $\gamma^2_{p_ip_j,s}$ as a function of $St$ for the lower cylinder at selected normalized spanwise spacings $\eta/D$. Surface pressure fluctuations at $\theta = 90$ deg were used to compute $\gamma^2_{p_ip_j,s}$ for both the single cylinder and the lower cylinder cases.**

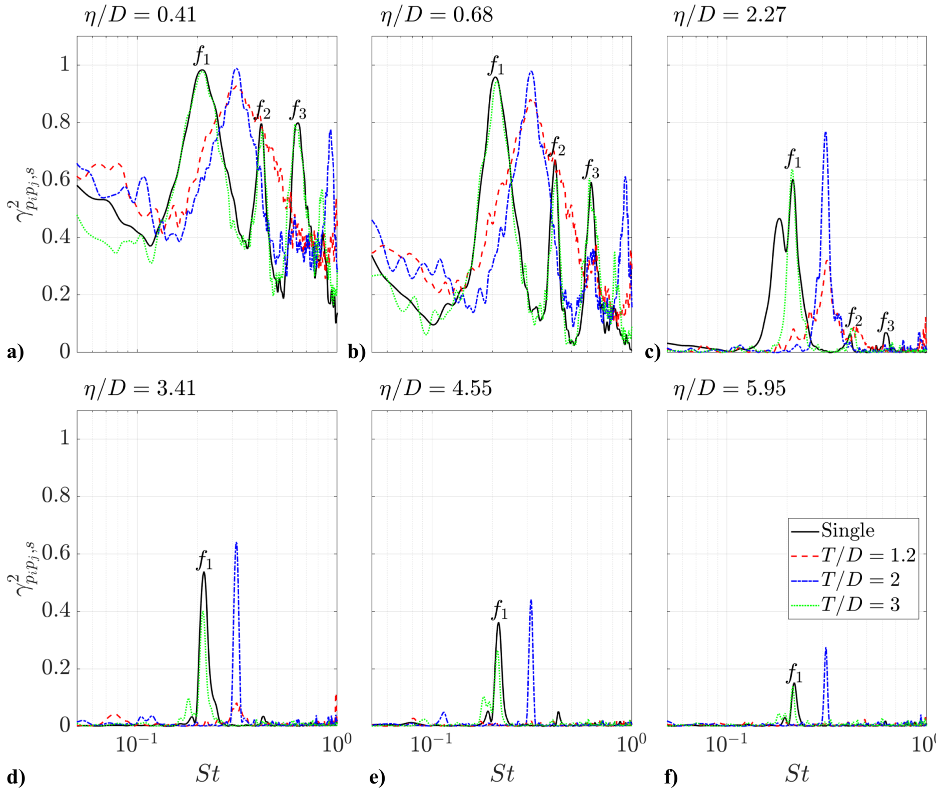


**Fig. 17 Spanwise coherence $\gamma^2_{p_i p_j, s}$ as a function of $St$ for the upper cylinder at selected normalized spanwise spacings $\eta/D$. Surface pressure fluctuations at $\theta = 90$ deg for the single cylinder and $\theta = 270$ deg for the upper cylinder were used to compute $\gamma^2_{p_i p_j, s}$.**

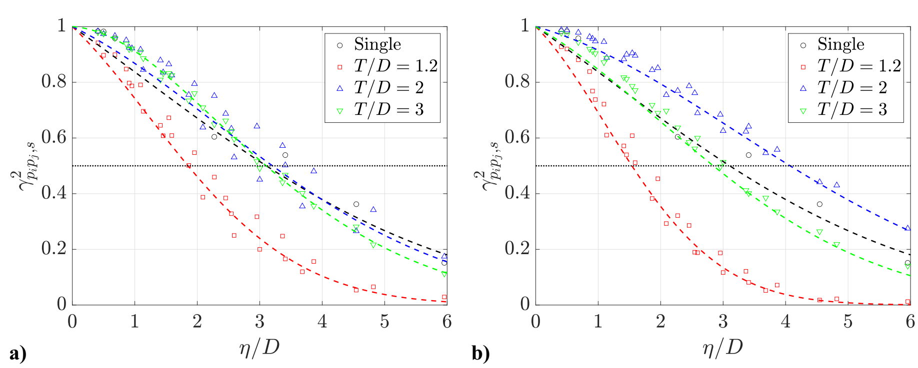


**Fig. 18 Spanwise coherence at the dominant-peak frequency (corresponding to the high-frequency peak for $T/D = 1.2$), as a function of normalized spanwise spacing $\eta/D$. Gaussian fits are shown as dashed lines. The coherence was extracted at a) $\theta = 90$ deg for the lower cylinder and b) $\theta = 270$ deg for the upper cylinder. For the single-cylinder case, coherence was also extracted at $\theta = 90$ deg.**

In this study, the magnitude of $\gamma^2_{p_i p_j, s}$ at the dominant-peak frequency, extracted from Fig. 18, was used to estimate the spanwise coherence length, denoted by $\Lambda$, following previous studies [24,30,61,62], using the relation

$$\Lambda = \int_0^{+\infty} \sqrt{\gamma^2_{p_i p_j, s}}\, \mathrm{d}\eta \tag{4}$$

Through a trial-and-error process, it was determined that the variation of the dominant peak magnitude with respect to $\eta/D$, as shown in Fig. 18, is best represented by a Gaussian decay distribution

$$G = a_1 \exp\left[-\left(\frac{\eta - b_1}{c_1}\right)^2\right] \tag{5}$$

where $a_1$, $b_1$, and $c_1$ are the fitted coefficients. In the absence of sufficient $\gamma^2_{p_i p_j, s}$ data at the dominant-peak frequency across the entire span, the Gaussian fit $G$ was numerically integrated instead of $\gamma^2_{p_i p_j, s}$ in Eq. (4) over the range $\eta/D = 0$ to 6 to estimate $\Lambda$. Using this method, as illustrated in Fig. 19, the spanwise correlation length for

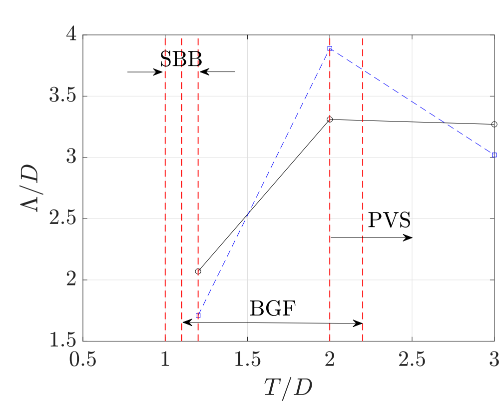


**Fig. 19 Variation of the spanwise coherence length $\Lambda$ at the dominant-peak frequency as a function of $T/D$. Black solid and blue dashed lines represent the lower and upper cylinders, respectively. Based on the gap flow behavior: single-bluff-body (SBB) behavior for $1 < T/D < 1.1$–$1.2$, BGF for $1.1$–$1.2 < T/D < 2$–$2.2$, and PVS for $T/D > 2$–$2.2$ [6].**

the single cylinder $\Lambda$ was found to be $3.25D$, which is consistent with the broader data set reported in the literature [30,33]. For the side-by-side configurations, at $T/D = 1.2$, $\Lambda$ decreases relative to the single cylinder, reaching $2.07D$ and $1.71D$ for the lower and upper cylinders, respectively. Increasing the spacing to $T/D = 2$ results in larger values, $3.31D$ and $3.89D$, while at $T/D = 3$, $\Lambda$ decreases again to $3.27D$ and $3.02D$, approaching that of the single cylinder. Notably, at $T/D = 1.2$, the upper cylinder exhibits a smaller $\Lambda$ than the lower cylinder, a trend that reverses at $T/D = 2$, consistent with the characteristics of the BGF regime.

## IV. Conclusions

This study experimentally investigated the near-field surface pressure characteristics and far-field noise of two identical circular cylinders arranged in a side-by-side configuration at $Re = 3.0 \times 10^4$ with spacing ratios ranging from $T/D = 1.2$–3. Two highly instrumented cylinders equipped with miniature pressure transducers were used to measure near-field surface pressure fluctuations along both the spanwise and azimuthal directions, while a set of microphones was employed for far-field noise measurements.

The results revealed that, similar to a single cylinder, the imposed pressure fluctuations on the surface of cylinders in side-by-side configurations contribute to dominant tonal noise. However, except for spacing ratios close to $T/D = 3$, which exhibited behavior comparable to the single-cylinder case, the other configurations, particularly at $T/D = 1.2$, demonstrated a noticeable reduction in tonal noise magnitude. This reduction was attributed to the suppression of surface pressure fluctuations and the shorter spanwise correlation of these fluctuations. Beyond changes in magnitude, the $T/D = 1.2$ configuration also produced multiple tones at frequencies both lower and higher than the single-cylinder tone. This behavior was associated with the highly unsteady and asymmetric wake resulting from gap-flow deflection and the formation of a biased-gap flow regime. The mean static pressure coefficient distribution supported this observation, showing that the front stagnation point and other critical angular locations shifted by approximately 20 deg, clockwise for the lower cylinder and counterclockwise for the upper cylinder. Consistent with the work of Alam and Zhou [54], the gap flow separated from the upper surface of the lower cylinder, impinged on the lower side of the upper cylinder, wrapped around it, and exited downstream. Consequently, the lower cylinder exhibited a wider wake region, causing drag reduction relative to the upper cylinder. This behavior was further supported by the near-field surface pressure directivity patterns, where the single-cylinder dipolelike distribution was replaced by an elliptical pattern, tilted clockwise around the lower cylinder and counterclockwise around the upper cylinder, highlighting the strong aerodynamic interference and 3D effects induced by the biased gap flow at smaller spacings.

## Acknowledgments

Paul Abromeit and Thomas F. Geyer thank Maximilian Prügel (Brandenburg University of Technology Cottbus–Senftenberg) for assistance with measurements and Stefan Rohark (Brandenburg University of Technology Cottbus–Senftenberg) for the fabrication of experimental components. The efforts of Reza Maryami and Brian R. Elbing were partially supported by the Gordon and Betty Moore Foundation (doi: 10.37807/GBMF11559).

## References

[1] Gerrard, J., "The Wakes of Cylindrical Bluff Bodies at Low Reynolds Number," *Philosophical Transactions of the Royal Society of London. Series A, Mathematical and Physical Sciences*, Vol. 288, No. 1354, 1978, pp. 351–382.
https://doi.org/10.1098/rsta.1978.0020

[2] Williamson, C. H., "Vortex Dynamics in the Cylinder Wake," *Annual Review of Fluid Mechanics*, Vol. 28, No. 1, 1996, pp. 477–539.
https://doi.org/10.1146/annurev.fl.28.010196.002401

[3] Zdravkovich, M., "Review of Flow Interference Between Two Circular Cylinders in Various Arrangements," *Journal of Fluids Engineering*, Vol. 99, No. 4, 1977, pp. 618–633.
https://doi.org/10.1115/1.3448871

[4] Zdravkovich, M., "The Effects of Interference Between Circular Cylinders in Cross Flow," *Journal of Fluids and Structures*, Vol. 1, No. 2, 1987, pp. 239–261.
https://doi.org/10.1016/S0889-9746(87)90355-0

[5] Zdravkovich, M., "Review and Classification of Various Aerodynamic and Hydrodynamic Means for Suppressing Vortex Shedding," *Journal of Wind Engineering and Industrial Aerodynamics*, Vol. 7, No. 2, 1981, pp. 145–189.
https://doi.org/10.1016/0167-6105(81)90036-2

[6] Sumner, D., "Two Circular Cylinders in Cross-Flow: A Review," *Journal of Fluids and Structures*, Vol. 26, No. 6, 2010, pp. 849–899.
https://doi.org/10.1016/j.jfluidstructs.2010.07.001

[7] Zhou, Y., and Alam, M. M., "Wake of Two Interacting Circular Cylinders: A Review," *International Journal of Heat and Fluid Flow*, Vol. 62, Dec. 2016, pp. 510–537.
https://doi.org/10.1016/j.ijheatfluidflow.2016.08.008

[8] Gu, Z., and Sun, T., "On Interference Between Two Circular Cylinders in Staggered Arrangement at High Subcritical Reynolds Numbers," *Journal of Wind Engineering and Industrial Aerodynamics*, Vol. 80, No. 3, 1999, pp. 287–309.
https://doi.org/10.1016/S0167-6105(98)00205-0

[9] Kiya, M., Arie, M., Tamura, H., and Mori, H., "Vortex Shedding from Two Circular Cylinders in Staggered Arrangement," *Journal of Fluids Engineering*, Vol. 102, No. 2, 1980, pp. 166–171.
https://doi.org/10.1115/1.3240637

[10] Igarashi, T., "Characteristics of the Flow Around Two Circular Cylinders Arranged in Tandem: 1st Report," *Bulletin of JSME*, Vol. 24, No. 188, 1981, pp. 323–331.
https://doi.org/10.1299/jsme1958.24.323

[11] Zdravkovich, M., and Pridden, D., "Interference Between Two Circular Cylinders; Series of Unexpected Discontinuities," *Journal of Wind Engineering and Industrial Aerodynamics*, Vol. 2, No. 3, 1977, pp. 255–270.
https://doi.org/10.1016/0167-6105(77)90026-5

[12] Sumner, D., Price, S., and Paidoussis, M., "Flow-Pattern Identification for Two Staggered Circular Cylinders in Cross-Flow," *Journal of Fluid Mechanics*, Vol. 411, May 2000, pp. 263–303.
https://doi.org/10.1017/S0022112099008137

[13] Hutcheson, F. V., and Brooks, T. F., "Noise Radiation from Single and Multiple Rod Configurations," *International Journal of Aeroacoustics*, Vol. 11, Nos. 3–4, 2012, pp. 291–333.
https://doi.org/10.1260/1475-472X.11.3-4.291

[14] Lockard, D., Khorrami, M., Choudhari, M., Hutcheson, F., Brooks, T., and Stead, D., "Tandem Cylinder Noise Predictions," *13th AIAA/CEAS Aeroacoustics Conference (28th AIAA Aeroacoustics Conference)*, AIAA Paper 2007-3450, 2007.
https://doi.org/10.2514/6.2007-3450

[15] Hutcheson, F. V., Brooks, T. F., Lockard, D. P., Choudhari, M. M., and Stead, D. J.Acoustics and Surface Pressure Measurements from Tandem Cylinder Configurations," *20th AIAA/CEAS Aeroacoustics Conference*, AIAA Paper 2014-2762, 2014.
https://doi.org/10.2514/6.2014-2762

[16] Geyer, T. F., and Enghardt, L., "Noise Generation by Two Staggered Circular Cylinders of Equal Diameter in Cross-Flow," *28th AIAA/CEAS Aeroacoustics 2022 Conference*, AIAA Paper 2022-3093, 2022.
https://doi.org/10.2514/6.2022-3093

[17] Maryami, R., Arcondoulis, E. J., Liu, Q., and Liu, Y., "Experimental Near-Field Analysis for Flow Induced Noise of a Structured Porous-Coated Cylinder," *Journal of Sound and Vibration*, Vol. 551, May 2023, Paper 117611.
https://doi.org/10.1016/j.jsv.2023.117611

[18] Maryami, R., Arcondoulis, E. J., and Liu, Y., "Flow and Aerodynamic Noise Control of a Circular Cylinder by Local Blowing," *Journal of Fluid Mechanics*, Vol. 980, Feb. 2024, Paper A56.
https://doi.org/10.1017/jfm.2024.39

[19] Maryami, R., Arcondoulis, E. J., Guo, J., and Liu, Y., "Experimental Investigation of Active Local Blowing on the Aerodynamic Noise Reduction of a Circular Cylinder," *Journal of Sound and Vibration*, Vol. 578, May 2024, Paper 118360.
https://doi.org/10.1016/j.jsv.2024.118360

[20] Maryami, R., and Liu, Y., "Cylinder Flow and Noise Control by Active Base Blowing," *Journal of Fluid Mechanics*, Vol. 985, April 2024, Paper A10.
https://doi.org/10.1017/jfm.2024.261

[21] Maryami, R., Guo, J., Naseer, M. R., and Liu, Y., "Vortex-Induced Noise Suppression of a Cylinder with Blowing Through Porous

Media," *Physics of Fluids*, Vol. 36, No. 6, 2024. https://doi.org/10.1063/5.0211397

[22] Oguma, Y., Yamagata, T., and Fujisawa, N., "Measurement of Sound Source Distribution Around a Circular Cylinder in a Uniform Flow by Combined Particle Image Velocimetry and Microphone Technique," *Journal of Wind Engineering and Industrial Aerodynamics*, Vol. 118, July 2013, pp. 1–11. https://doi.org/10.1016/j.jweia.2013.04.003

[23] Maryami, R., Showkat Ali, S. A., Azarpeyvand, M., and Afshari, A., "Turbulent Flow Interaction with a Circular Cylinder," *Physics of Fluids*, Vol. 32, No. 1, 2020, Paper 015105. https://doi.org/10.1063/1.5119967

[24] Maryami, R., and Ali, S. A. S., "Near-Field Pressure and Wake Velocity Coherence of a Circular Cylinder," *Physics of Fluids*, Vol. 35, No. 11, 2023. https://doi.org/10.1063/5.0174931

[25] Jenkins, L., Neuhart, D., McGinley, C., Khorrami, M., and Choudhari, M., "Measurements of Unsteady Wake Interference Between Tandem Cylinders," *36th AIAA Fluid Dynamics Conference and Exhibit*, AIAA Paper 2006-3202, 2006. https://doi.org/10.2514/6.2006-3202

[26] Ljungkrona, L., and Sundén, B., "Flow Visualization and Surface Pressure Measurement on Two Tubes in an Inline Arrangement," *Experimental Thermal and Fluid Science*, Vol. 6, No. 1, 1993, pp. 15–27. https://doi.org/10.1016/0894-1777(93)90037-J

[27] Ljungkrona, L., Norberg, C., and Sundén, B., "Free-Stream Turbulence and Tube Spacing Effects on Surface Pressure Fluctuations for Two Tubes in an In-Line Arrangement," *Journal of Fluids and Structures*, Vol. 5, No. 6, 1991, pp. 701–727. https://doi.org/10.1016/0889-9746(91)90364-U

[28] Maryami, R., Ali, S. A. S., Azarpeyvand, M., Dehghan, A. A., and Afshari, A., "The Influence of Cylinders in Tandem Arrangement on Unsteady Aerodynamic Loads," *Experimental Thermal and Fluid Science*, Vol. 139, Nov. 2022, Paper 110709. https://doi.org/10.1016/j.expthermflusci.2022.110709

[29] Maryami, R., Showkat Ali, S. A., and Elbing, B., "Experimental Investigation of Near-Field Surface Pressure Characteristics of Two Side-by-Side Cylinders," *AIAA Aviation Forum and Ascend*, AIAA Paper 2025-3690, 2025. https://doi.org/10.2514/6.2025-3690

[30] Maryami, R., Azarpeyvand, M., Dehghan, A., and Afshari, A., "An Experimental Investigation of the Surface Pressure Fluctuations for Round Cylinders," *Journal of Fluids Engineering*, Vol. 141, No. 6, 2019. https://doi.org/10.1115/1.4042036

[31] Sarradj, E., Fritzsche, C., Geyer, T., and Giesler, J., "Acoustic and Aerodynamic Design and Characterization of a Small-Scale Aeroacoustic Wind Tunnel," *Applied Acoustics*, Vol. 70, No. 8, 2009, pp. 1073–1080. https://doi.org/10.1016/j.apacoust.2009.02.009

[32] West, G., and Apelt, C., "The Effects of Tunnel Blockage and Aspect Ratio on the Mean Flow Past a Circular Cylinder with Reynolds Numbers Between $10^4$ and $10^5$," *Journal of Fluid Mechanics*, Vol. 114, Jan. 1982, pp. 361–377. https://doi.org/10.1017/S0022112082000202

[33] Norberg, C., "Fluctuating Lift on a Circular Cylinder: Review and New Measurements," *Journal of Fluids and Structures*, Vol. 17, No. 1, 2003, pp. 57–96. https://doi.org/10.1016/S0889-9746(02)00099-3

[34] Goody, M. C., and Simpson, R. L., "An Experimental Investigation of Pressure Fluctuations in Three-Dimensional Turbulent Boundary Layers," Ph.D. Thesis, Dept. of Aerospace and Ocean Engineering, 1999.

[35] Corcos, G., "Resolution of Pressure in Turbulence," *Journal of the Acoustical Society of America*, Vol. 35, No. 2, 1963, pp. 192–199. https://doi.org/10.1121/1.1918431

[36] Bearman, P., and Wadcock, A., "The Interaction Between a Pair of Circular Cylinders Normal to a Stream," *Journal of Fluid Mechanics*, Vol. 61, No. 3, 1973, pp. 499–511. https://doi.org/10.1017/S0022112073000832

[37] Kim, H.-J., and Durbin, P., "Investigation of the Flow Between a Pair of Circular Cylinders in the Flopping Regime," *Journal of Fluid Mechanics*, Vol. 196, Nov. 1988, pp. 431–448. https://doi.org/10.1017/S0022112088002769

[38] Alam, M. M., Moriya, M., and Sakamoto, H., "Aerodynamic Characteristics of Two Side-by-Side Circular Cylinders and Application of Wavelet Analysis on the Switching Phenomenon," *Journal of Fluids and Structures*, Vol. 18, Nos. 3–4, 2003, pp. 325–346. https://doi.org/10.1016/j.jfluidstructs.2003.07.005

[39] Guillaume, D., and LaRue, J., "Investigation of the Flopping Regime with Two-, Three- and Four-Cylinder Arrays," *Experiments in Fluids*, Vol. 27, No. 2, 1999, pp. 145–156. https://doi.org/10.1007/s003480050339

[40] Spivack, H. M., "Vortex Frequency and Flow Pattern in the Wake of Two Parallel Cylinders at Varied Spacing Normal to an Air Stream," *Journal of the Aeronautical Sciences*, Vol. 13, No. 6, 1946, pp. 289–301. https://doi.org/10.2514/8.11375

[41] Kamemoto, K., "Formation and Interaction of Two Parallel Vortex Streets," *Bulletin of JSME*, Vol. 19, No. 129, 1976, pp. 283–290. https://doi.org/10.1299/jsme1958.19.283

[42] Bernard, P. S., and Handler, R. A., "Reynolds Stress and the Physics of Turbulent Momentum Transport," *Journal of Fluid Mechanics*, Vol. 220, Nov. 1990, pp. 99–124. https://doi.org/10.1017/S0022112090003202

[43] Thomas, D. G., and Kraus, K. A., "Interaction of Vortex Streets," *Journal of Applied Physics*, Vol. 35, No. 12, 1964, pp. 3458–3459. https://doi.org/10.1063/1.1713250

[44] Zhou, Y., Wang, Z., So, R., Xu, S., and Jin, W., "Free Vibrations of Two Side-by-Side Cylinders in a Cross-Flow," *Journal of Fluid Mechanics*, Vol. 443, Sept. 2001, pp. 197–229. https://doi.org/10.1017/S0022112001005171

[45] Williamson, C., "Evolution of a Single Wake Behind a Pair of Bluff Bodies," *Journal of Fluid Mechanics*, Vol. 159, Oct. 1985, pp. 1–18. https://doi.org/10.1017/S002211208500307X

[46] Zhou, Y., Zhang, H., and Yiu, M., "The Turbulent Wake of Two Side-by-Side Circular Cylinders," *Journal of Fluid Mechanics*, Vol. 458, May 2002, pp. 303–332. https://doi.org/10.1017/S0022112002007887

[47] Gloerfelt, X., Pérot, F., Bailly, C., and Juvé, D., "Flow-Induced Cylinder Noise Formulated as a Diffraction Problem for Low Mach Numbers," *Journal of Sound and Vibration*, Vol. 287, Nos. 1–2, 2005, pp. 129–151. https://doi.org/10.1016/j.jsv.2004.10.047

[48] Inoue, O., and Hatakeyama, N., "Sound Generation by a Two-Dimensional Circular Cylinder in a Uniform Flow," *Journal of Fluid Mechanics*, Vol. 471, Nov. 2002, pp. 285–314. https://doi.org/10.1017/S0022112002002124

[49] Sadeh, W. Z., and Saharon, D. B., "Turbulence Effect on Crossflow Around a Circular Cylinder at Subcritical Reynolds Numbers," NASA CR 3622, Nov. 1982.

[50] Fage, A., and Falkner, V., "Further Experiments on the Flow Around a Circular Cylinder," H. M. Stationery Office R&M 1369 (Ae. 496), 1931, https://reports.aerade.cranfield.ac.uk/handle/1826.2/1416.

[51] Zdravkovich, M., "Flow Induced Oscillations of Two Interfering Circular Cylinders," *Journal of Sound and Vibration*, Vol. 101, No. 4, 1985, pp. 511–521. https://doi.org/10.1016/S0022-460X(85)80068-7

[52] Norberg, C., and Sunden, B., "Turbulence and Reynolds Number Effects on the Flow and Fluid Forces on a Single Cylinder in Cross Flow," *Journal of Fluids and Structures*, Vol. 1, No. 3, 1987, pp. 337–357. https://doi.org/10.1016/0889-9746(87)90264-7

[53] Norberg, C., "Effects of Reynolds Number and a Low-Intensity Freestream Turbulence on the Flow Around a Circular Cylinder," Chalmers Univ., Technological Publications TR 87/2, Goteborg, Sweden, May 1987, pp. 1–55.

[54] Alam, M. M., and Zhou, Y., "Flow Around Two Side-by-Side Closely Spaced Circular Cylinders," *Journal of Fluids and Structures*, Vol. 23, No. 5, 2007, pp. 799–805. https://doi.org/10.1016/j.jfluidstructs.2006.12.002

[55] Norberg, C., "Interaction Between Freestream Turbulence and Vortex Shedding for a Single Tube in Cross-Flow," *Journal of Wind Engineering and Industrial Aerodynamics*, Vol. 23, 1986, pp. 501–514. https://doi.org/10.1016/0167-6105(86)90066-8

[56] Casalino, D., and Jacob, M., "Prediction of Aerodynamic Sound from Circular Rods via Spanwise Statistical Modelling," *Journal of Sound and Vibration*, Vol. 262, No. 4, 2003, pp. 815–844. https://doi.org/10.1016/S0022-460X(02)01136-7

[57] Glegg, S., and Devenport, W., *Aeroacoustics of Low Mach Number Flows: Fundamentals, Analysis, and Measurement*, Academic Press, London, 2017.

[58] Weidman, P. D., "Wake Transition and Blockage Effects on Cylinder Base Pressures," Ph.D. Thesis, California Inst. of Technology, California, 1968.

[59] Norberg, C., "Pressure Distributions Around a Circular Cylinder in Cross-Flow," *Symposium on Bluff Body Wakes and Vortex-Induced Vibrations (BBVIV3)*, Monash Univ., Melbourne, Australia, 2002, pp. 17–20.

[60] Etkin, B., Korbacher, G., and Keefe, R. T.Acoustic Radiation from a Stationary Cylinder in a Fluid Stream (Aeolian Tones)," *Journal of the Acoustical Society of America*, Vol. 29, No. 1, 1957, pp. 30–36. https://doi.org/10.1121/1.1908673

[61] Xiang, Z., Arcondoulis, E., Maryami, R., and Liu, Y., "Spanwise Coherence Measurements of Porous Coated Cylinders in Uniform Flow," *INTER-NOISE and NOISE-CON Congress and Conference Proceedings*, Vol. 265, Inst. of Noise Control Engineering, Washington, D.C., 2022, pp. 772–783.

[62] Margnat, F., da Silva Pinto, W. J. G., and Noûs, C., "Cylinder Aeroacoustics: Experimental Study of the Influence of Cross-Section Shape on Spanwise Coherence Length," *Acta Acustica*, Vol. 7, Jan. 2023, p. 4. https://doi.org/10.1051/aacus/2022061

X. Zhang
*Associate Editor*